Chemical Engineering Journal 505 (2025) 159130

Contents lists available at ScienceDirect

Chemical Engineering Journal

journal homepage: www.elsevier.com/locate/cej

Sustainable solar-driven interfacial evaporation-photocatalytic degradation of Cu-ZIF-67/rGO/PVA aerogel: A multifunctional material for pollutant treatment

Fan Nie [a,1], Jihai Cai [a,b,1], Lingxuan Ma [a], Sheng Gong [a], Shuangpeng Wang [c], Wenqian Chen [d], Shengliang Li [e,*], Jinchao Wei [a,*], Peng Li [a,*]

[a] Macau Centre for Research and Development in Chinese Medicine, State Key Laboratory of Quality Research in Chinese Medicine, Institute of Chinese Medical Sciences, University of Macau, Macau 999078, China
[b] State Key Laboratory of Pulp and Paper Engineering, South China University of Technology, 381 Wushan Road, Guangzhou 510640, China
[c] Institute of Applied Physics and Materials Engineering, University of Macau, Macau 999078, China
[d] Department of Pharmacy and Pharmaceutical Sciences, National University of Singapore, Science Drive 4, 117560, Singapore
[e] College of Pharmaceutical Sciences, Soochow University, Suzhou 215123, China

ARTICLE INFO

Keywords:
Solar-driven degradation
Photocatalysis
Interfacial evaporation
Metal-Organic Framework
Alternating hydrophilic/hydrophobic structure

ABSTRACT

Simultaneously satisfying recovery and efficient degradation remains a challenge for photocatalysis in pollutant treatment. Hence, Cu-ZIF-67 loaded rGO/PVA aerogel (Cu-ZIF-67/rGO/PVA) is prepared by thermal reduction and surface growth, which boosts photocatalytic rate of recyclable aerogel by utilizing concomitant heat to enhance mass transfer by interfacial evaporation. The Cu ions doping of ZIF-67 advances the overlapping of its absorption band with sunlight and accelerates the separation of the photogenerated hole-electron. PVA based aerogel provides mechanical strength for loading and recycling of Cu-ZIF-67. rGO provides an excellent conductive substrate to extract and transport charge carriers to the reaction site while enhancing solar energy absorption and interfacial evaporation efficiencies. The evaporation rate of Cu-ZIF-67/rGO/PVA could reach 1.95 kg m^{-2} h^{-1} under 1 kW m^{-2} simulated solar illumination, and the photothermal conversion efficiency could reach 92.1%. Highly efficient thermal conversion promotes rapid localized warming of the Cu-ZIF-67/rGO/PVA, accelerating the production of reactive oxidants and enhancing their reactivity. Under one solar intensity, the degradation of MB by Cu-ZIF-67/rGO/PVA was significantly improved, increasing from 14.79% to 78.52%. Moreover, Cu-ZIF-67/rGO/PVA has excellent salt resistance. Therefore, Cu-ZIF-67/rGO/PVA shows strong potential for synergistic photocatalytic degradation of organic pollutants via interfacial evaporation, providing a novel approach for complex pollutant treatment.

1. Introduction

Dye pollution from textile, printing, and dyeing industries is bringing huge ecological pressure to global water bodies, which has adverse effects on aquatic and terrestrial organisms and human health [1–3]. As the center of global textile production, China is particularly prone to dye pollution [4]. Therefore, timely and effective treatment of dye contamination is important to ensure the health of water bodies, protect the ecological environment, and safeguard public health [5–7].

Photocatalytic degradation technology has attracted much attention due to its significant advantages of being green, efficient degradation, and no fossil energy consumption [8–10]. In recent decades, numerous photocatalysts such as metal oxides, metal-organic frameworks (MOFs), and graphene-based materials have been developed for photodegradation [11–14]. ZIF-67 (zeolite imidazolium framework-67) is a kind of metal-organic framework (MOF) composed of cobalt ions and imidazolium ligands with a stable chemical structure [15,16]. The cobalt ions in ZIF-67 act as active centers capable of generating photogenerated electrons and holes in response to light, and these active sites contribute to redox reactions [17]. In addition, the suitable band gap of ZIF-67 (Eg = 1.90 eV) makes it an effective visible light photocatalyst [18,19]. Cu doping can further broaden the light absorption range of

* Corresponding authors.
E-mail addresses: lishengliang@suda.edu.cn (S. Li), wjc551@hotmail.com, jinchaowei@um.edu.mo (J. Wei), pli1978@hotmail.com, pengli@um.edu.mo (P. Li).
[1] Author has the same share as the first author.

https://doi.org/10.1016/j.cej.2024.159130

Available online 30 December 2024

ZIF-67 and generate more electron-hole pairs under the light while retaining the porous structure, which significantly improves the efficiency of photocatalytic degradation [20,21]. However, the persistence of nanomaterials like ZIF-67 in the environment after photodegradation usually exacerbates long-term damage to the ecosystem[22]. They are difficult to degrade naturally and will continue to produce free radicals under sunlight, which affects the normal growth of microorganisms, plants, and animals in water and soil. He et al. found that adsorption of nanophotonic catalysts onto the surface of embryos resulted in direct nanobiotic interactions that caused the generation of ROS, leading to increased mortality [23]. The coexistence of transition metal-containing photocatalysts, influenced by external energy sources, induces significant chemical changes. These processes contribute to the production and stabilization of environmentally persistent free radicals (EPFRs). EPFRs can enter the body through various pathways, stimulating reactive oxygen species production and increasing the risk of cardiorespiratory diseases [24]. Such impacts not only disturb the ecological balance but also lead to a cumulative effect of pollutants in the environment [23,24].

Unlike nanoparticles, bulk materials are easier to recover and reuse. Among them, PVA aerogels are widely applied for photocatalytic degradation by loading photocatalysts due to their lightweight, porous structure and good chemical stability. Meanwhile, the floating of PVA aerogels enables facile recycling. Furthermore, dispersing of TiO_2 [25], ZnO [26], and metal-organic framework (MOF) [27,28], etc. in the PVA matrix enhances their dispersion and stability. However, aerogels and the nanoparticles they contain can not disperse evenly and contact with pollutants as well as only nanoparticles in water body. The reaction rate of ROS generated in photocatalysis is fast but the diffusion distance is extremely short, emphasising that the pollutant must be close to the catalyst surface in order to react efficiently [29]. Inspired by the sunlight-induced transpiration in plants as a way to transport nutrients to the crown, it is proposed that if the aerogels can evaporate water, the mass transfer of pollutants will be accelerated to photocatalytic active sites [30–36]. Meanwhile, heat inevitably dissipated by part of absorbed photon energy during photocatalysis is utilized. With high photothermal conversion efficiency, the temperature of the reaction system is well elevated. As the temperature of the system increases, the generation of active oxidants accelerates, while their reactivity is also significantly enhanced, thus promoting the reaction process more effectively [37,38]. Therefore, by combining photocatalytic degradation and thermal evaporation, this multifunctional aerogel is hypothesized to enhance the overall effect of water purification through improving the efficiency of pollutant degradation [39].

Herein, as illustrated in Fig. 1, Cu-ZIF-67/rGO/PVA aerogels were designed and prepared to improve the overall interfacial photocatalytic properties. Firstly, reducing graphene oxide (rGO) was integrated into PVA aerogels to provide good electrical conductivity, which enabled the rapid transfer of photogenerated electrons from Cu-ZIF-67 to the reaction interface. Meanwhile, rGO has a wide range of light absorption, so it can efficiently convert light into heat through photothermal conversion. Subsequently, Cu-ZIF-67 was loaded on rGO/PVA aerogel by *in situ* growth in a solution containing cobalt (II), copper (II), and 2-methylimidazole. By combining interfacial evaporation with photocatalysis, Cu-ZIF-67/rGO/PVA drove water evaporation under sunlight to enrich pollutants on its surface and efficiently degraded them, achieving significantly enhanced pollutant capture and detoxification. Compared with traditional photocatalysis, this method improves the efficiency of photocatalytic reaction, shortens reaction time, and shows advantages in energy consumption, providing a promising new way to treat organic pollutants in water.

2. Experimental section

2.1. Material and Characterization

This section is provided in the Supplementary Information (S1, S2).

2.2. Preparation of materials

PVA: In a typical synthesis, PVA (1 g), glutaraldehyde (125 μL, 50% wt in DI water), and DI water (10 mL) were mixed by sonication.

rGO/PVA aerogel: Mix 2 mL of 2 mg/mL GO dispersion evenly with 2 mL of the prepared PVA stock solution. The rGO/PVA mixed suspension was ultrasonically treated for about 30 min to ensure that GO was evenly dispersed. An appropriate amount of ascorbic acid was added to the GO suspension, and ultrasonication was continued for 20 min. The mixed solution was then placed in an oven and heated to 80°C, and the reaction was continued for 2 h. The prepared gel was soaked in deionized water for 24 h to remove residual ascorbic acid and by-products. The rGO/PVA was then frozen at -80°C refrigerator overnight, and then freeze-dried for 48 h to obtain rGO/PVA aerogel (Fig. S13a & d).

ZIF-67/rGO/PVA aerogel: Take 2 mL of 2 mg/mL GO dispersion and

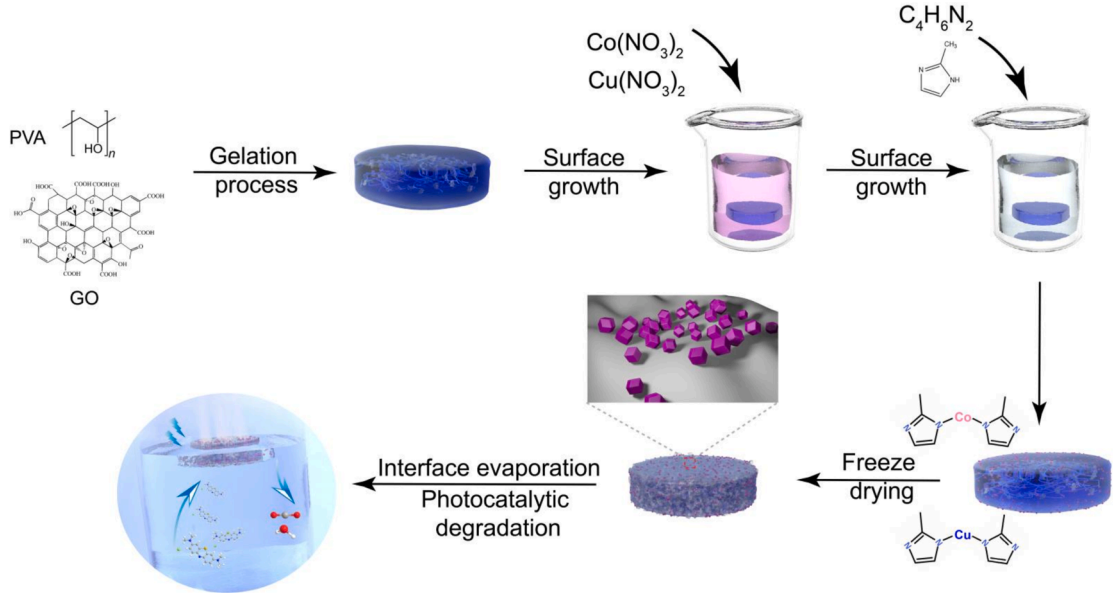

Fig. 1. Schematic illustration of the formation of Cu-ZIF-67/rGO/PVA and its interfacial evaporation-photocatalysis synergistic water treatment.

mix it evenly with 2 mL of prepared PVA stock solution. The rGO/PVA mixed suspension was ultrasonically treated for about 30 min to ensure that GO was evenly dispersed. Add an appropriate amount of ascorbic acid to the GO suspension and continue ultrasonication for 20 min. Then, put the mixed solution into an oven, heat it to 80°C, and continue the reaction for 2 h. Soak the prepared gel in deionized water for 24 h to remove residual ascorbic acid and by-products. Place the rGO/PVA hydrogel in 50 mL, 10.2 mg/L $Co(NO_3)_2$ solution and stir it magnetically for 24 h, then place it in 50 mL of 22.4 mg/L 2-methylimidazole solution and stir it magnetically for 24 h. Put the ZIF-67/rGO/PVA into an -80°C refrigerator and freeze it overnight. They were then freeze-dried for 48 h to obtain an aerogel of ZIF-67 grown on rGO/PVA surface (ZIF-67/rGO/PVA) (Fig. S13b & e).

Cu-ZIF-67/rGO/PVA aerogel: Take 2 mL of 2 mg/mL GO dispersion and mix it evenly with 2 mL of prepared PVA stock solution. The rGO/PVA mixed suspension was ultrasonically treated for about 30 min to ensure that GO was evenly dispersed. Add an appropriate amount of ascorbic acid to the GO suspension and continue ultrasonication for 20 min. Put the mixed solution into an oven, heat it to 80°C, and continue the reaction for 2 h. Soak the prepared gel in deionized water for 24 h to remove residual ascorbic acid and by-products. Place the rGO/PVA hydrogel in 50 mL of solution containg 10.2 mg/L $Co(NO_3)_2$ and 1 mg/L $Cu(NO_3)_2$, then stir magnetically for 24 h, then place it in 50 mL, 22.4 mg/L 2-methylimidazole solution and stir it magnetically for 24 h. Put the Cu-ZIF-67/rGO/PVA into a -80°C refrigerator and freeze it overnight. They were then freeze-dried for 48 h to obtain an aerogel of Cu-ZIF-67 grown on rGO/PVA surface (Cu-ZIF-67/rGO/PVA) (Fig. S13c & f).

2.3. Water evaporation and photocatalytic performance measurement

Simulate sunlight by a solar simulator (Beijing Newbit HSX-F/UV300 xenon light source solar simulator) using an AM 1.5 G filter. Zhongjiao Jinyuan CEL-NP2000-2A fully automatic optical power meter tests sunlight intensity. The water evaporation rate was measured using an electronic scale (JA203N, analytical electronic balance, Changzhou Lucky Electronic Equipment Co., Ltd., China), and real-time data was collected at 1 point every 10 min. Infrared photos were taken and recorded with a Fluke TiS55+ thermal imager. This uses a data logging thermometer (NTC, 10 K/3435) to measure the temperature. All experiments were typically performed at an ambient temperature of 24°C (Evaporation enthalpy tests and related calculations are provided in S3).

A methylene blue aqueous solution with a concentration of 10 mg/L was used as the target pollutant for photocatalytic degradation. The photocatalyst was placed in 50 mL of 10 mg/L MB solution. First, the adsorption reaction was carried out for 1 h. After the adsorption was balanced, the xenon lamp was turned on, and the sample concentration changes were tested every 20 min. Changes in MB concentration were measured by absorbance during the photocatalytic process using a DR6000 visible spectrophotometer (MB degradation-related calculations are provided in S4).

3. Results and Discussion

Reduced graphene oxide (rGO) is suitable for pollutant degradation due to its broadband absorption of light and high chemical stability, which effectively capture light energy and enhance the efficiency of photocatalysis [40]. Based on the basic principles of “water transportation” and “water evaporation” theory, according to the spectral absorption and heat transfer effect of Cu-ZIF-67 and rGO, Cu-ZIF-67/rGO/PVA which combined solar-driven interfacial evaporation and photocatalyst was designed and synthesized. PVA and rGO form a cross-linked interpenetrating porous network structure in this reaction system, and Cu-ZIF-67 grows on its surface. While achieving photocatalytic degradation, it also conducts rapid enrichment of pollutants, which greatly reduces the mass transfer limitations.

3.1. Characterization of photothermal-photocatalytic Cu-ZIF-67/rGO/PVA

Scanning electron microscope (SEM) images of rGO/PVA, ZIF-67/rGO/PVA, and Cu-ZIF-67/rGO/PVA are shown in Fig. 2a-c. The surface of the rGO/PVA aerogel exhibits a microscopic porous structure with cladding of smooth rGO nanosheets. After loading, the ZIF-67 or Cu-ZIF-67 is tightly bound to rGO/PVA to form a composite structure. Since rGO/PVA aerogels have a porous structure and Cu-ZIF-67 has a microporous structure and grows on their surface, Cu-ZIF-67/rGO/PVA (108.79 m^2/g) exhibits a larger specific surface area than rGO/PVA (23.07 m^2/g), providing more active sites for adsorption and catalysis. In addition, the synergistic effect of the multilevel pore structure (micro- and mesopores) improved the adsorption capacity and photocatalytic efficiency [41]. Atomic force microscopy (AFM) tests are shown in Fig. 2d-f, reflecting the minor undulations and irregularities of the rGO/PVA, ZIF-67/rGO/PVA, and Cu-ZIF-67/rGO/PVA surfaces. rGO/PVA, ZIF-67/rGO/PVA, and Cu-ZIF-67/rGO/PVA have root-mean-square roughnesses (Rq) of 4.74, 5.03, and 17.1 nm, respectively. Larger roughnesses usually imply a larger surface area, which can provide more adsorption sites and thus enhance the adsorption effect, and this result is also consistent with the BET results. The structure and morphology of Cu-ZIF-67/rGO/PVA obtained by SEM analysis are shown in Fig. 2g-l. C, N, Co, Cu, and O elements are evenly distributed on the surface of Cu-ZIF-67/rGO/PVA.

The crystallized phases of rGO/PVA, ZIF-67/rGO/PVA, and Cu-ZIF-67/rGO/PVA were further validated by XRD. As shown in Fig. 3a, XRD spectra of rGO/PVA show that the characteristic peaks of rGO appeared at 23.5° (2θ), 43° (2θ) corresponding to the (002), (100) crystal planes of rGO. PVA showed three characteristic diffraction peaks at 19.5° (2θ), 38.7° (2θ), 43° (2θ). With the addition of rGO, diffraction peaks from rGO/PVA show some overlap, suggesting an interfacial interaction between rGO and the PVA matrix [42]. Characteristic diffraction peaks belonging to ZIF-67 and Cu-ZIF-67 (7.3° (001), 10.5° (002), 12.7° (112), 16.6° (013), 18.3° (222), 22.3° (114), 24.7° (233), 26.7° (134) and 30.2° (044) were observed in the XRD spectra of ZIF-67/rGO/PVA and Cu-ZIF-67/rGO/PVA (Fig. 3a inset). The results showed that ZIF-67 and Cu-ZIF-67 were successfully loaded onto the surface of rGO. For the larger ionic radius of Cu^{2+} (0.073 nm) than Co^{2+} (low spin 0.065 nm), when Cu replace some Co in ZIF-67, blue shift of the XRD diffraction peaks was occurred in Cu-ZIF-67/rGO/PVA compared with ZIF-67/rGO/PVA (Fig. 3a) [43]. The distortion of the Cu-ZIF-67/rGO/PVA diffraction peaks and the weakening of the relative intensities also indicate that the crystal structure and orientation of ZIF-67 have changed after the Cu atoms have replaced part of the Co atoms (inset of Fig. 3a). Due to the monolayer or few-layer structure of rGO, its diffraction properties may have masked some of the diffraction peaks of ZIF-67 and Cu-ZIF-67, which may be attributed to the high surface area and layered structure of rGO limiting the crystal diffraction signals of the composites. The elemental composition and surface chemical state of the rGO/PVA, ZIF-67/rGO/PVA, and Cu-ZIF-67/rGO/PVA were determined by XPS (X-ray photoelectron spectroscopy). As shown in Fig. 3b, rGO/PVA is composed of C and O, and the peaks of C 1s spectrum at 284.8 eV and 286.2 eV correspond to C= C/C-C and C-O bonds, respectively (Fig. S1). ZIF-67/rGO/PVA comprises four elements: C, N, O, and Co, with contents of 61.79%, 15.27%, 18.53%, and 4.40%, respectively. C 1s XPS spectrum at 285.7 eV shows a characteristic peak for C-N bonds in ZIF-67 (Fig. S2a). The N 1s XPS spectrum displays three nitrogen signals at 398.5 eV, 399.0 eV, and 400.2 eV, corresponding to pyridine N, pyrrole N, and Co-N, respectively (Fig. S2b). The peaks in the Co 2p spectrum at 781.5 eV and 797.3 eV, corresponding to Co 2P3/2 and 2P1/2, respectively (Fig. 3c). Cu-ZIF-67/rGO/PVA is mainly composed of C, N, O, Co, and Cu, with contents of 67.77%, 7.71%, 21.69%, 2.27%, and 0.57%, respectively. C 1s XPS spectra at 285.3 eV also show a characteristic peak for C-N bonds in Cu-ZIF-67 (Fig. S3). The peaks in N 1s XPS spectrum at 398.4 eV, 398.8 eV, and 399.6 eV were assigned to

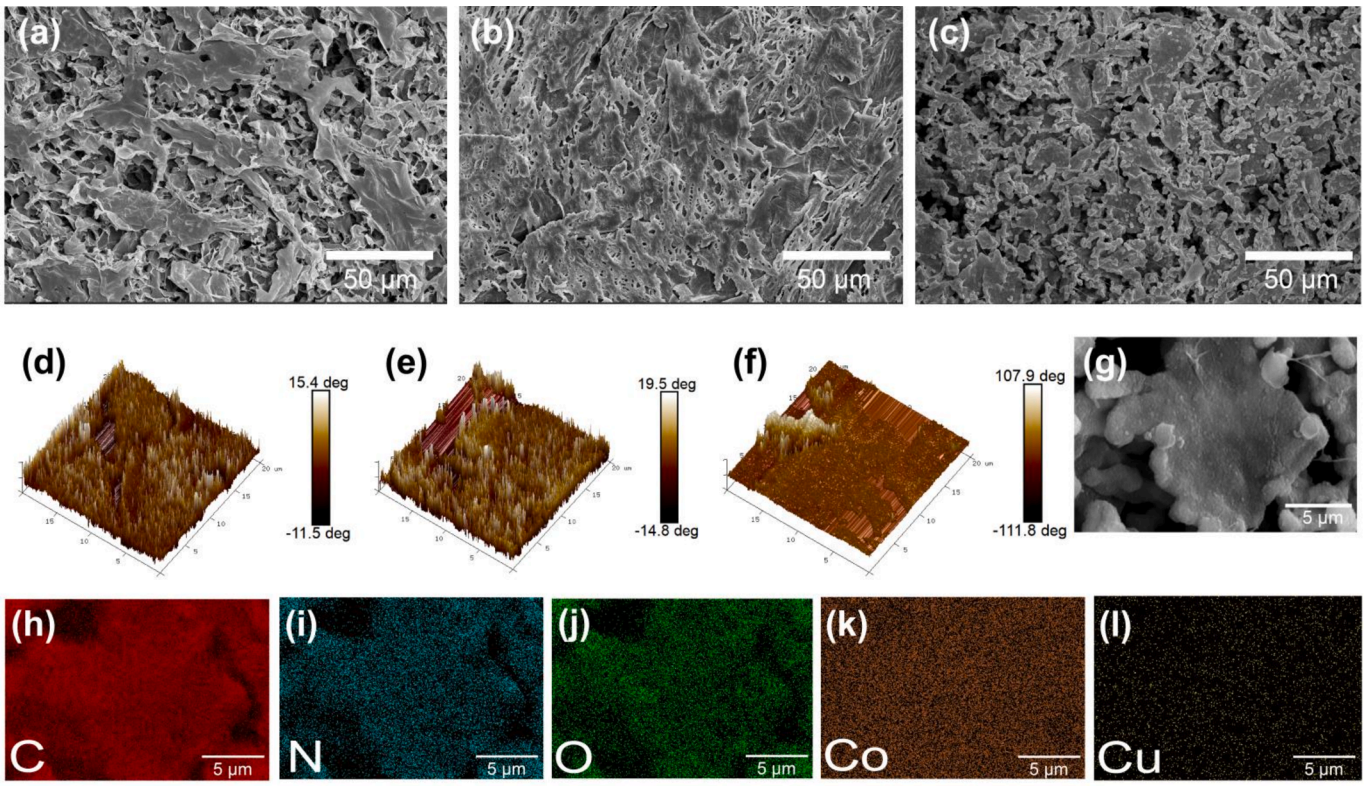

Fig. 2. Characterization of the hydrogel evaporators, SEM image of a) rGO/PVA, b) ZIF-67/rGO/PVA, c) Cu-ZIF-67/rGO/PVA, AFM image of d) rGO/PVA, e) ZIF-67/rGO/PVA, f) Cu-ZIF-67/rGO/PVA, g-l) SEM-EDS elemental mapping of the Cu-ZIF-67/rGO/PVA.

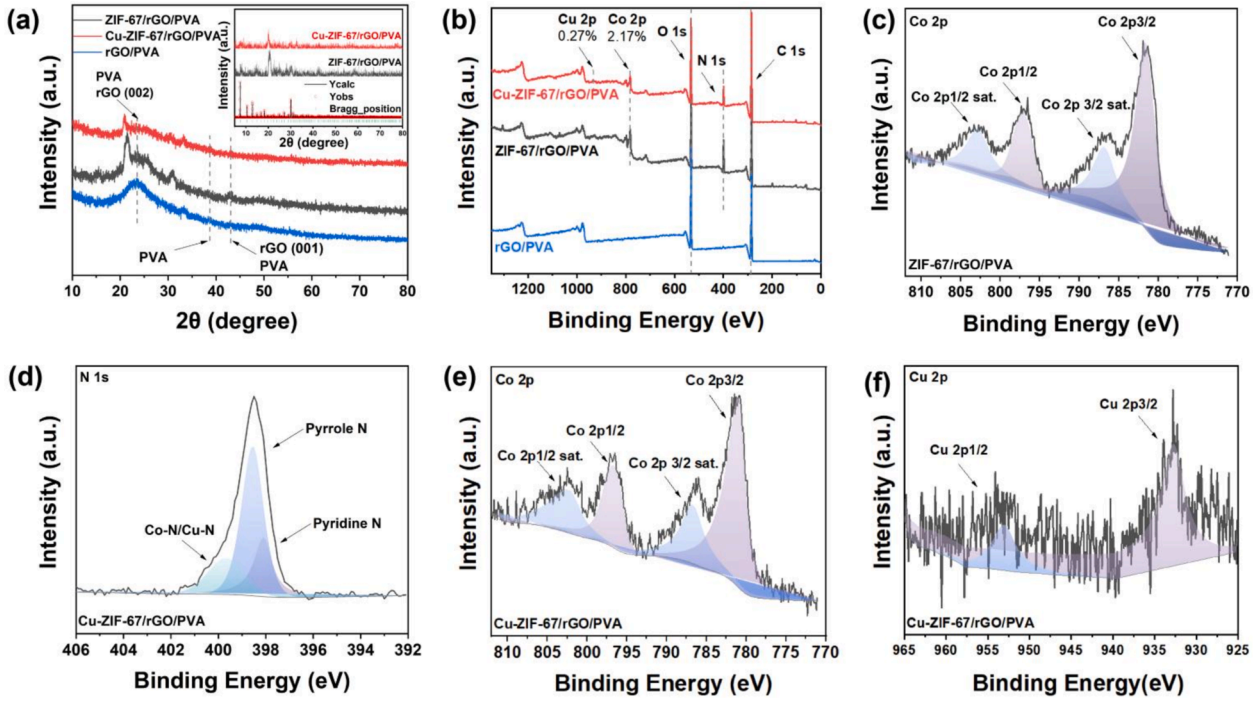

Fig. 3. a) XRD pattern of rGO/PVA, ZIF-67/rGO/PVA, Cu-ZIF-67/rGO/PVA, b) XPS full survey spectra of rGO/PVA, ZIF-67/rGO/PVA, Cu-ZIF-67/rGO/PVA, c) Co 2p XPS curves of ZIF-67/rGO/PVA, d) N 1 s XPS curves of Cu-ZIF-67/rGO/PVA, e) Co 2p XPS curves of Cu-ZIF-67/rGO/PVA, f) Cu 2p XPS curves of Cu-ZIF-67/rGO/PVA.

pyridine N, pyrrole N, and Co-N (Fig. 3d). The Co 2p spectrum shows two peaks at 781.5 eV and 797.3 eV, corresponding to Co 2P3/2 and 2P1/2, respectively (Fig. 3e). The Cu 2p spectrum shows two peaks at 932.7 eV, and 952.8 eV, corresponding to Cu 2P3/2 and 2P1/2 (Fig. 3f). After the introduction of Cu to form Cu-ZIF-67/rGO/PVA, the metal-N peak was observed to shift from 400.2 eV to a lower binding energy

(399.6 eV). Cu atoms replaced a portion of the Co atoms in the ZIF-67 structure, thereby forming a Cu-N bond. After Cu replaced Co, the interaction between the Cu-N bonds was weaker, and the electron density around the N atoms increased, leading to the moving of the N 1 s peak toward a lower binding energy. The thermal degradation processes of rGO/PVA, ZIF-67/rGO/PVA, and Cu-ZIF-67/rGO/PVA in a nitrogen atmosphere were investigated by simultaneous thermal analysis to explore their thermal stability. Fig. S4 & Fig. 4a shows the TG and DTG curves for rGO/PVA, ZIF-67/rGO/PVA, and Cu-ZIF-67/rGO/PVA. Between 0°C and 100°C, the mass of these samples decreased slightly, probably due to the release of adsorbed water or volatiles. From 200°C to 500°C, the mass decreases rapidly, especially between 300°C and 400°C, suggesting that the main components decompose in this temperature range. Between 500°C and 800°C, the weight change levels off and the remainder is a thermally stable residue. Compared with rGO/PVA and ZIF-67/rGO/PVA, it can be clearly seen that the TG curves of Cu-ZIF-67/rGO/PVA shifted to the low-temperature region. The reaction rate of the DTG curves was obviously increased, which indicated that the addition of Cu-ZIF-67 catalyzed the oxidation of the Cu-ZIF-67/rGO/PVA reaction with an elevated reaction rate. Compared with ZIF-67/rGO/PVA, the addition of Cu shifted the TG curves of ZIF-67/rGO/PVA to the low-temperature region. The DTG curves showed significantly higher reaction rates, indicating that adding Cu produced a catalytic effect and promoted the oxidation reaction of Cu-ZIF-67/rGO/PVA with an elevated reaction rate. rGO/PVA, ZIF-67/rGO/PVA, and Cu-ZIF-67/rGO/PVA were characterized by specific surface area testing (Fig. S5 & Fig. 4b). rGO/PVA had a BET-specific surface area of 23.07 m^2 g^{-1} and a pore volume of 0.059 cm^3 g^{-1}, and the adsorption isothermal curves showed mesoporous adsorption characteristics, with a pore size mainly between 2 and 100 nm. The specific surface area of ZIF-67/rGO/PVA was 105.80 m^2 g^{-1}, and the pore volume was 0.057 cm^3 g^{-1}. The specific surface area of Cu-ZIF-67/rGO/PVA was further increased to 108.79 m^2 g^{-1}, and the pore volume was 0.0623 cm^3 g^{-1}. Loading Cu-ZIF-67 into rGO/PVA enhanced the specific surface area and pore volume of Cu-ZIF-67/rGO/PVA. The pore size distribution map showed that the pore size migrated from the larger mesoporous region (~10.24 nm) to the microporous region (~2.29 nm) with the introduction of Cu-ZIF-67.

3.2. Evaporation performance based on photothermal conversion

The design of this simulating solar-driven interfacial evaporation experiment is shown in Fig. 5a. Mass of water vapor and temperature of rGO/PVA, ZIF-67/rGO/PVA, and Cu-ZIF-67/rGO/PVA surface is measured by an electronic analytical balance and an infrared camera, respectively. The Cu-ZIF-67/rGO/PVA aerogel was placed on top of polyethylene foam to reduce heat transfer underneath the aerogel towards the bulk water. The interfacial evaporation of rGO/PVA, ZIF-67/rGO/PVA, and Cu-ZIF-67/rGO/PVA were initially investigated under 1.0 solar radiation. The Cu-ZIF-67/rGO/PVA exhibited the highest solar evaporation rate of 1.95 kg m^{-2} h^{-1}, among that of the ZIF-67/rGO/PVA (1.75 kg m^{-2} h^{-1}), rGO/PVA (1.69 kg m^{-2} h^{-1}) and PVA (0.53 kg m^{-2} h^{-1}) (Fig. 5b). The evaporation rates of rGO/PVA, ZIF-67/rGO/PVA, and Cu-ZIF-67/rGO/PVA under various light intensities were investigated, as illustrated in Fig. S6. The evaporation rates of rGO/PVA were measured to be 1.69, 4.69, and 7.16 kg m^{-2} h^{-1} for 1, 3, and 5 solar radiations, respectively, and the evaporation rates of ZIF-67/rGO/PVA were 1.75, 5.53 and 8.15 kg m^{-2} h^{-1} for 1, 3 and 5 solar radiations, respectively. The evaporation rates of Cu-ZIF-67/rGO/PVA under 1, 3, and 5 solar irradiations were 1.95, 6.44, and 9.47 kg m^{-2} h^{-1}, respectively. Under the dry state, surface temperature of the rGO/PVA composite rapidly increased from 26°C to 65.2°C within 30 s, and then slowly increased to 76.3°C and remained stable. In comparison, the surface temperature of ZIF-67/rGO/PVA increased from 26°C to 60.1°C within 30 s and then gradually increased to 69.7°C and stabilized. For Cu-ZIF-67/rGO/PVA, the surface temperature increases from 26°C to 61.2°C within 30 s, and then gradually rises to 73.3°C before stabilizing. (Fig. S7). The thermal conductivity of polyethylene foam is $\leq$ 0.03720 W/mK [44], while that of Cu-ZIF-67/rGO/PVA were 0.05552 W/mK, 0.05091 W/mK, and 0.05050 W/mK at 25°C, 45°C, and 65°C, respectively (Fig. S8). Polyethylene foam has excellent thermal insulation properties due to its lower thermal conductivity and can be effectively placed between Cu-ZIF-67/rGO/PVA and the water body to reduce heat dissipation. The use of polyethylene foam in this experiment allows the concentration of heat and increasing of temperature in the upper region where Cu-ZIF-67/rGO/PVA aerogel contacts with water. The IR camera images of rGO/PVA, ZIF-67/rGO/PVA, and Cu-ZIF-67/rGO/PVA are shown in Fig. 4c-e. In the wet state, the warming behavior of rGO/PVA, ZIF-67/rGO/PVA, and Cu-ZIF-67/

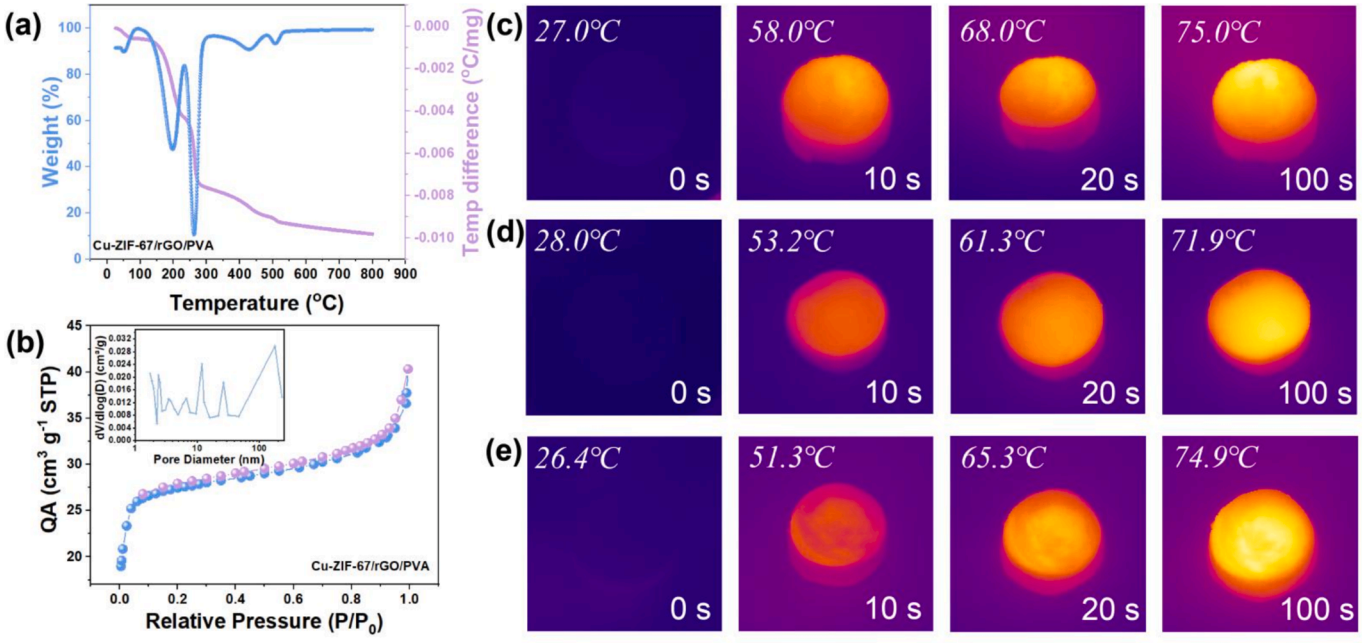

Fig. 4. TG-DTG curves of a) Cu-ZIF-67/rGO/PVA, BET curves of b) Cu-ZIF-67/rGO/PVA(QA: quantity adsorbed), IR images of the surface of the c) rGO/PVA, d) ZIF-67/rGO/PVA, e) Cu-ZIF-67/rGO/PVA under 1 sun irradiation.

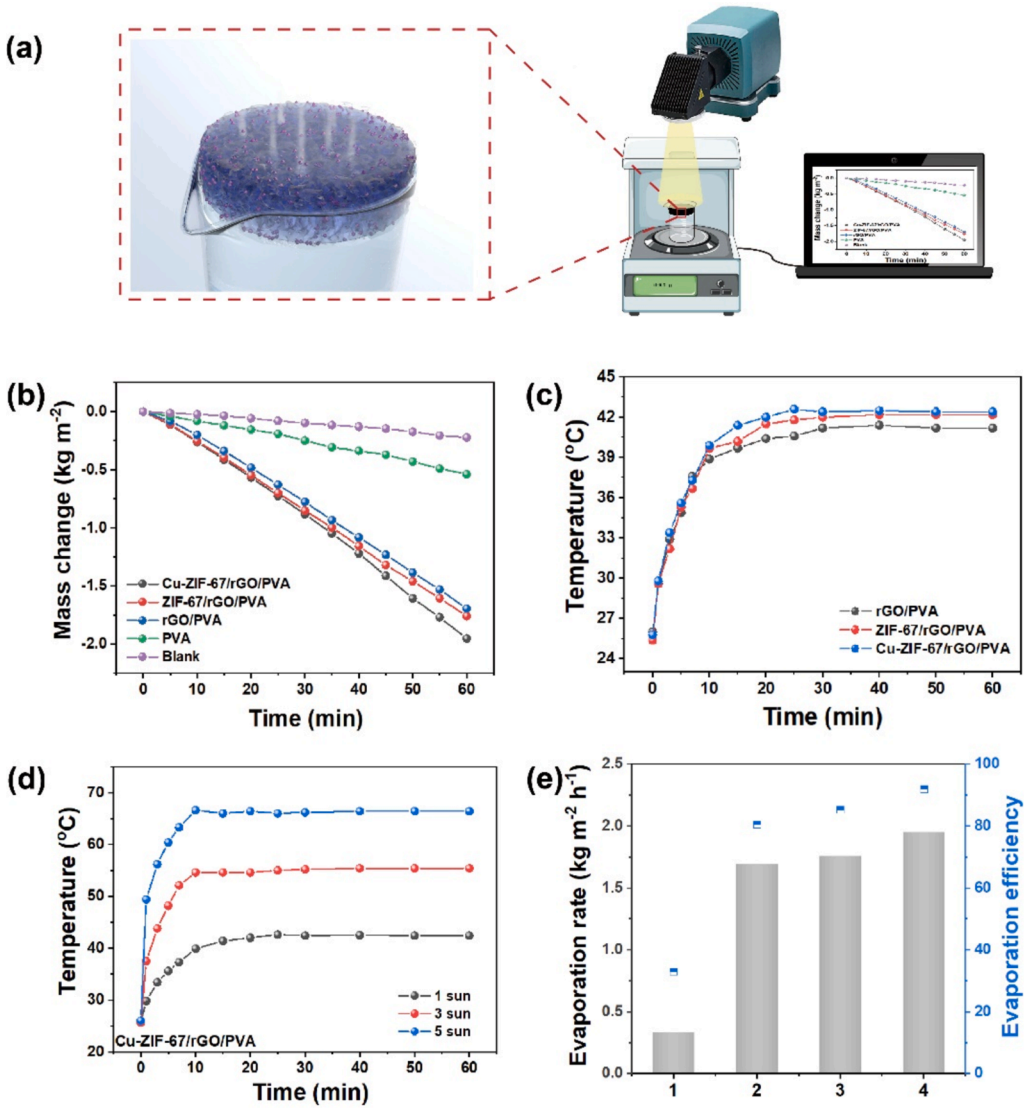

Fig. 5. a) schematic representation of the interfacial solar-driven vapor generation experimental setup, b) mass loss of water with rGO/PVA, ZIF-67/rGO/PVA, Cu-ZIF-67/rGO/PVA under 1.0 sun, c) surface temperature curves of rGO/PVA, ZIF-67/rGO/PVA, Cu-ZIF-67/rGO/PVA under 1 sun illumination during interfacial evaporation, d) temperature curves of Cu-ZIF-67/rGO/PVA under 1, 3, 5 sun illumination, e) Equivalent vaporization enthalpy of bulk water and water in rGO/PVA, ZIF-67/rGO/PVA, Cu-ZIF-67/rGO/PVA (Note: 1-Blank, 2-rGO/PVA, 3-ZIF-67/rGO/PVA, 4-Cu-ZIF-67/rGO/PVA).

rGO/PVA surface may be influenced by moisture and thus exhibit different temperature change characteristics. The surface temperatures of rGO/PVA, ZIF-67/rGO/PVA, and Cu-ZIF-67/rGO/PVA increased to 41.2°C, 42°C, and 42.4°C, respectively, within 10 min and remained stable under the intensity of 1 sunlight (Fig. 5c). Cu-ZIF-67/rGO/PVA rapidly warmed up to 42.4°C within 10 min in the light, and the rate of warming increased with the light intensity increased, and to 66.4°C by five sunlight irradiations. The temperature remained stable after 20 min, demonstrating the excellent performance of the photothermal. This proves that the photothermal conversion performance of Cu-ZIF-67/rGO/PVA is excellent (Fig. 5d).

The enthalpy of evaporation of bulk water at room temperature is 2450 kJ kg^{-1}. According to Eq. 2-2, the enthalpies of evaporation of water on rGO/PVA, ZIF-67/rGO/PVA and Cu-ZIF-67/rGO/PVA surfaces were 1989.6, 1839.4, and 1638.4 kJ kg^{-1}, respectively (Fig. 5e). The oxygen-containing functional groups on PVA reduce the enthalpy of evaporation by rearranging the interactions between the water molecules, thus increasing the efficiency of water evaporation. The growth of hydrophilic ZIF-67 on hydrophobic rGO generates alternating hydrophilic and hydrophobic structures. In addition, the oxygen electron pair in the water molecule can form a coordination bond with the uncoordinated Co^{2+}. This coordination disrupts and disorganizes the hydrogen bond distribution of water. In Cu-ZIF-67/rGO/PVA, introducing copper alters the strength of hydrogen bonding with the imidazolium nitrogen atoms, which may further reduce the enthalpy of evaporation of water molecules [45]. The evaporation rates of rGO/PVA, ZIF-67/rGO/PVA, and Cu-ZIF-67/rGO/PVA evaporators at 1× light intensity were 1.69, 1.75, and 1.95 kg m^{-2} h^{-1}. According to Eq. 2-3, the corresponding evaporation efficiencies were 80.5%, 85.3%, and 92.1%, respectively (Fig. 5e) [46]. To investigate long-term stability, the evaporation rate of the Cu-ZIF-67/rGO/PVA was measured in 32 cycles of solar radiation (1 h each, four days) (Fig. S9). The slight daily fluctuations in the evaporation rate were attributed to variations in ambient humidity. In addition, no significant shape change was observed on Cu-ZIF-67/rGO/PVA, which indicates that the Cu-ZIF-67/rGO/PVA has excellent cycling stability. Additionally, the salt suppression property of the Cu-ZIF-67/rGO/PVA is one of the very important factors in the continuous evaporation process. Salt crystals precipitating on the evaporator's surface can cover the light-absorbing layer and pores, reducing the efficiency of light and heat conversion and blocking the escape channels for water vapor.

Hence, Cu-ZIF-67/rGO/PVA was placed in simulated seawater for a 7 h long-term salt tolerance test to assess its stability in a saline environment. The results are shown in Fig. S10, where no salt crystals were deposited on the upper surface of the Cu-ZIF-67/rGO/PVA in this successive test. Cu-ZIF-67/rGO/PVA composite demonstrates excellent stability during cycling. It also maintains excellent performance in high-salt environments. The interior has a rich three-dimensional interconnected pore structure. The three-dimensional network structure provides abundant water transmission channels, which allows the salt crystals on the surface to dissolve quickly; and the concentration gradient formed between the evaporator and the main water causes the salt ions to diffuse into the main water [47]. The outstanding performance of Cu-ZIF-67/rGO/PVA in terms of reuse and salt resistance shows its great potential for application.

3.3. Photodegradation of organic dye under simulated sunlight

The photocatalytic ability of Cu-ZIF-67/rGO/PVA was evaluated by photodegradation experiments in 10 mg/L (50 mL) MB solution as organic dye wastewater under 1 kW m^{-2} simulated sunlight. Under 1 kW m^{-2} light without a catalyst, the degradation rate of MB was only 15% after 180 min. However, in the presence of Cu-ZIF-67/rGO/PVA, the degradation rate of MB reached 78.52% in the same period, significantly higher than that of the pure dye without Cu-ZIF-67/rGO/PVA (Fig. 6a). The kinetics of catalytic degradation were analyzed as shown in Fig. S11, Table S2. Fitting of the experimental data revealed that the degradation process conformed to a pseudo-primary reaction kinetic model, The reaction rate constants for each material show that Cu-ZIF-67/rGO/PVA (0.00946 min^{-1}) > rGO/PVA (0.00738 min^{-1}) ≈ ZIF-67/rGO/PVA (0.00712 min^{-1}) > MB Only (0.000756 min^{-1}). The results showed that Cu-ZIF-67/rGO/PVA exhibited the highest reaction rate constants in the catalytic degradation experiments. As shown in Table S3, the photocatalysts designed in this study were able to achieve degradation comparable to other studies despite the limitation of light conditions. The changes of UV-vis absorption spectra during the photodegradation of MB solution at different reaction times are shown in Fig. 6b. As the reaction progressed, the characteristic peaks of MB gradually decreased, indicating that Cu-ZIF-67/rGO/PVA effectively degraded the organic pollutants under simulated solar radiation. The image of MB before and after photocatalytic degradation is shown in inset of Fig. 6a. In addition, Cu-ZIF-67/rGO/PVA can effectively degrade organic dyes such as MB, CV, and RhB, providing a promising way to obtain clean water (Fig. 6c). The effect of Cu-ZIF-67/rGO/PVA on MB degradation under different light intensities (Fig. 6d). The gradual increase in degradation rate with increasing light intensity (from 1 kW m^{-2} to 4 kW m^{-2}) suggests that higher light intensity helps to stimulate more photogenerated electron-hole pairs, which improves the efficiency of the photocatalytic reaction. Fig. 6e shows the catalytic performance of Cu-ZIF-67/rGO/PVA at different starting pH values which was adjusted by NaOH (0.1 M) or HCl (0.1 M). In the initial pH range of 7–11, the degradation efficiency of Cu-ZIF-67/rGO/PVA on MB was more than 80%. Moreover, at pH = 9 and 11, the degradation of MB could reach 80.89% and 83.8% within 100 min. However, the degradation efficiency of Cu-ZIF-67/rGO/PVA for MB decreased significantly when the initial pH value was below 7. The degradation rates of MB were only 55.21% and 69.3% at pH = 3 and pH = 5 within 180 min. Under the alkaline condition, the negative charge on the surface of Cu-ZIF-67/rGO/PVA increased, which was conducive to the adsorption of MB in the cationic state. The enhancement of interaction between Cu-ZIF-67/rGO/PVA and MB promoted its degradation reaction. The free radical quenching results indicate that $O_2^{\cdot-}$ was the main reactive oxidant in this reaction system. In order to test the degradation effect of Cu-ZIF-67/rGO/PVA on pollutants under real environmental conditions, photocatalytic degradation experiments were carried out for two consecutive hours in a natural environment (The experimental location was under full exposure to natural light to facilitate the simulation of photocatalytic effects in a real environment). The degradation rates of MB and CV by Cu-ZIF-67/rGO/PVA composites were 72.08% and 87.25%,

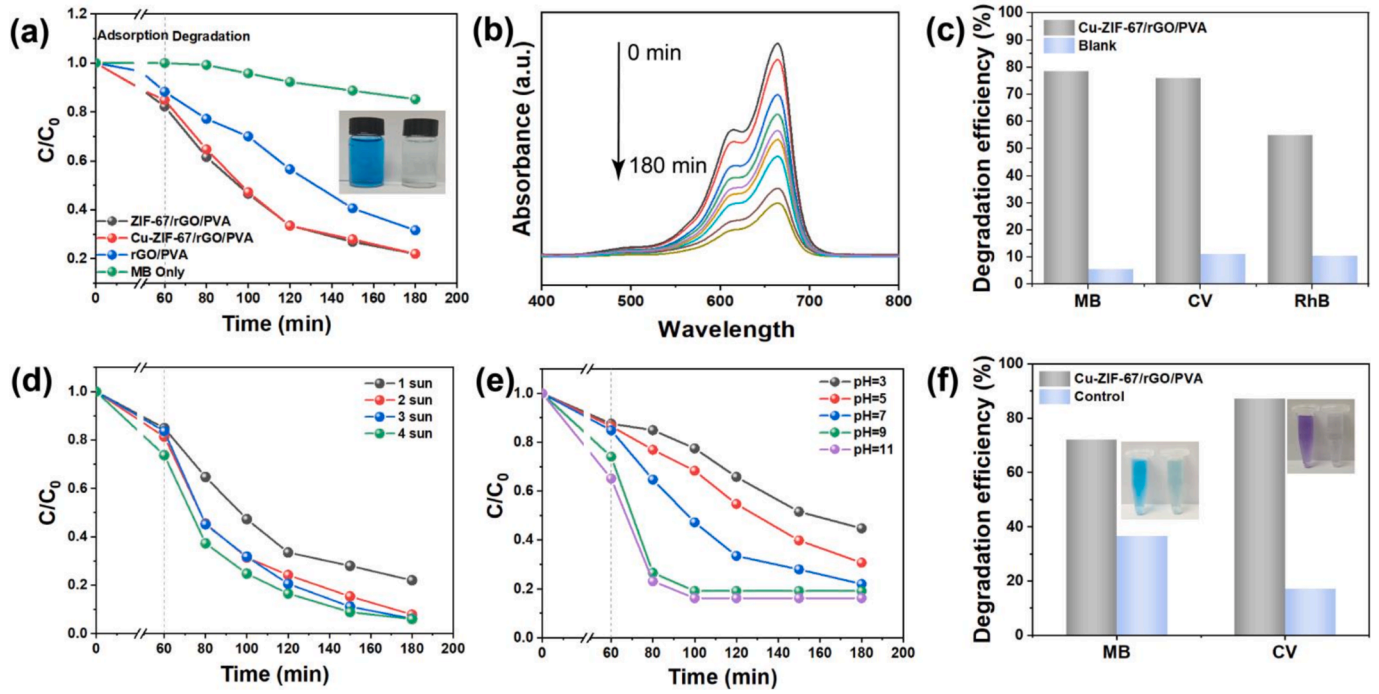

Fig. 6. a) photocatalytic degradation of mb by rGO/PVA, ZIF-67/rGO/PVA, Cu-ZIF-67/rGO/PVA, b) absorption intensity of mb solutions at different light times, c) degradation efficiency of mb, CV and RhB with or without the addition of Cu-ZIF-67/rGO/PVA (Reaction conditions: MB (5 mg/L, 50 mL), CV (5 mg/L, 50 mL), RhB (5 mg/L, 50 mL); light intensity: 1 solar intensity; reaction time: 1 h), d) Photocatalytic degradation of MB by Cu-ZIF-67/rGO/PVA under different light conditions, e) Photocatalytic degradation of MB by Cu-ZIF-67/rGO/PVA under different pH conditions, f) Photocatalytic degradation of MB, CV by Cu-ZIF-67/rGO/PVA under real illumination conditions. (For interpretation of the references to colour in this figure legend, the reader is referred to the web version of this article.)

respectively, in 120 min under real light conditions. Therefore, Cu-ZIF-67/rGO/PVA exhibited considerable photocatalytic degradation under laboratory environment and real conditions, showing its efficient degradation ability in various application scenarios and proving its reliability and practicality in practical water treatment (Fig. 6f). In order to investigate the performance of Cu-ZIF-67/rGO/PVA aerogels in seawater, we performed photocatalytic degradation tests in simulated seawater [48]. As shown in Fig. S12, the natural photodegradation rate of MB was only 19.9%, whereas the rate increased to 55.6% in the presence of Cu-ZIF-67/rGO/PVA. Compared with the performance in water (78.52%), the present of salt reduced 29.19% of catalytic activity, due to the Cl^- in simulated seawater may reduce generation of free radicals generated by reaction with electrons and holes while competed with MB for reactive sites [49]. Nevertheless, the result showed that Cu-ZIF-67/rGO/PVA was still effective in increasing the photodegradation rate in the presence of Cl^- [50,51].

3.4. Photocatalyst degradation mechanism

Free radicals play a crucial role in the photocatalytic degradation process and directly affect the degradation efficiency of pollutants. To further investigate the contribution of each ROS in photocatalytic process of Cu-ZIF-67/rGO/PVA, methanol, EDTA-2Na, and p-benzoquinone (BQ) were used as trapping agents for $HO^·$, h^+, and $O_2^{·-}$, respectively. The photodegradation efficiency of MB by Cu-ZIF-67/rGO/PVA without scavengers was 78.52%. When methanol, BQ, and EDTA-2Na were added as quenching agents, the photocatalytic degradation efficiency decreased to 64.46%, 71.06%, and 45.78%, respectively (Fig. 7a). The calculated contributions of $HO^·$, h^+, and $O_2^{·-}$ in MB degradation were 17.9%, 9.49%, and 41.69%, respectively. The cumulative contribution of the various reactive species is less than 100%, possibly because photogenerated electrons (e^-) can react directly with pollutants in a reductive manner and not through the free radical pathway. The results showed that $O_2^{·-}$ was the main active oxidant in the MB photocatalytic degradation process. This also explains the poorer degradation under strongly acidic conditions, since under strongly acidic conditions $O_2^{·-}$ is less stable and reactive, and it is easier to form hydrogen peroxide or other forms of neutral peroxides. EPR further identifies active oxidants in the photocatalytic degradation process, the free radicals of the reaction system were captured with DMPO, TEMP, and TPMPO. The obvious DMPO-$O_2^{·-}$ and DMPO-OH peaks did not appear under dark conditions but emerged after 10 min light radiation. The EPR results confirmed that the Cu-ZIF-67/rGO/PVA composites generated active species ($O_2^{·-}$, h^+, and $HO^·$) during the photocatalytic degradation process, which effectively promoted the degradation of pollutants (Fig. 7b-d) [52]. For the photocatalytic mechanism of Cu-ZIF-67/rGO/PVA, the generation and action of free radicals in the photocatalytic process were firstly confirmed by free radical trapping experiments. Based on this finding, UV-vis DRS and XPS valence band spectrum were further investigated to deeply explore photocatalytic mechanism. The light absorption at room temperature was analyzed by ultraviolet-visible diffuse reflectance spectroscopy (UV-vis DRS), and their band gap values were extrapolated. The results of the absorption spectra are shown in Fig. 8a-b. ZIF-67/RGO/PVA shows absorption of sunlight in the visible light of 200-350 nm and 450-650 nm, while the Cu doping in ZIF-67 enhances the absorption intensity in 350-500 nm and 650-2500 nm. The absorption peaks after 1500 nm are lower for ZIF-67/rGO/PVA and Cu-ZIF-67/rGO/PVA, but they are still consistent with the characteristic absorption peaks of rGO. The above results show that the absorption after 1500 nm is mainly contributed by rGO, and the influence of other components is negligible. The variation of absorption fringes indicates that the introduction of Cu significantly affects the electronic structure and optical properties of ZIF-67/RGO/PVA. ZIF-67/RGO/PVA has significant absorption fringes in the UV region, whereas the absorption fringes of Cu-ZIF-67/RGO/PVA have been slightly modulated and have new absorption properties in the visible range. These changes contribute to the

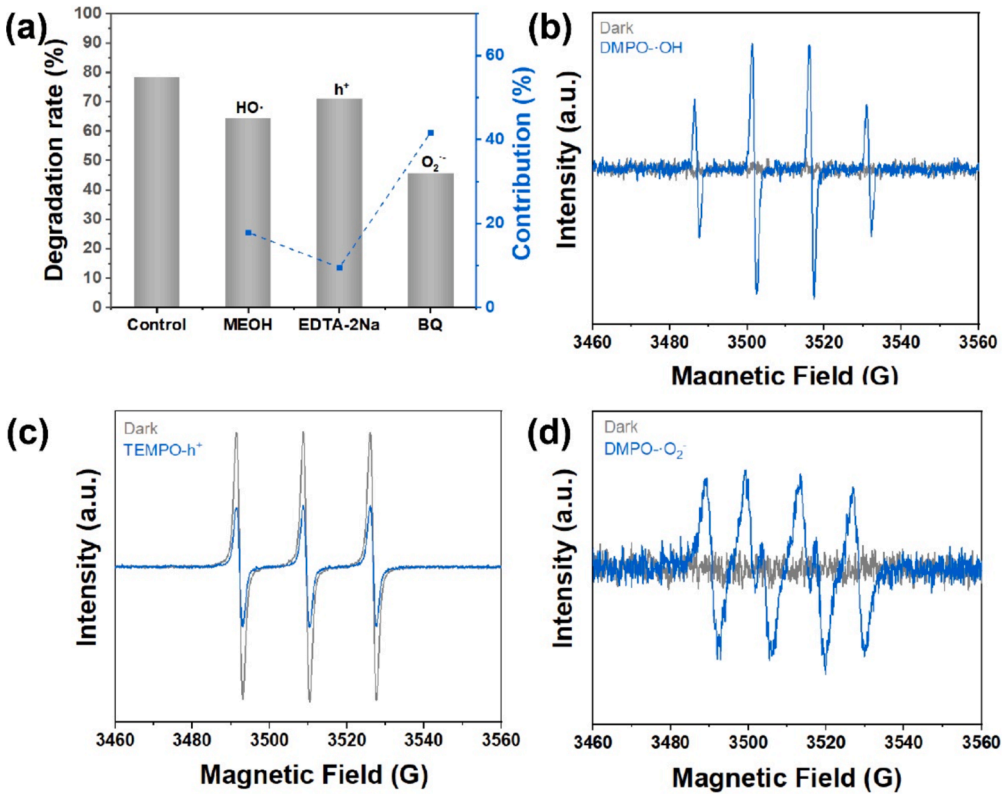

Fig. 7. a) photocatalytic degradation of MB on Cu-ZIF-67/rGO/PVA by different scavengers and the relative contribution of different active oxygen radicals, b-d) EPR spectra of DMPO-OH adduct, TEMPO-h^+ adduct and DMPO-$O_2^{·-}$ adduct for Cu-ZIF-67/rGO/PVA.

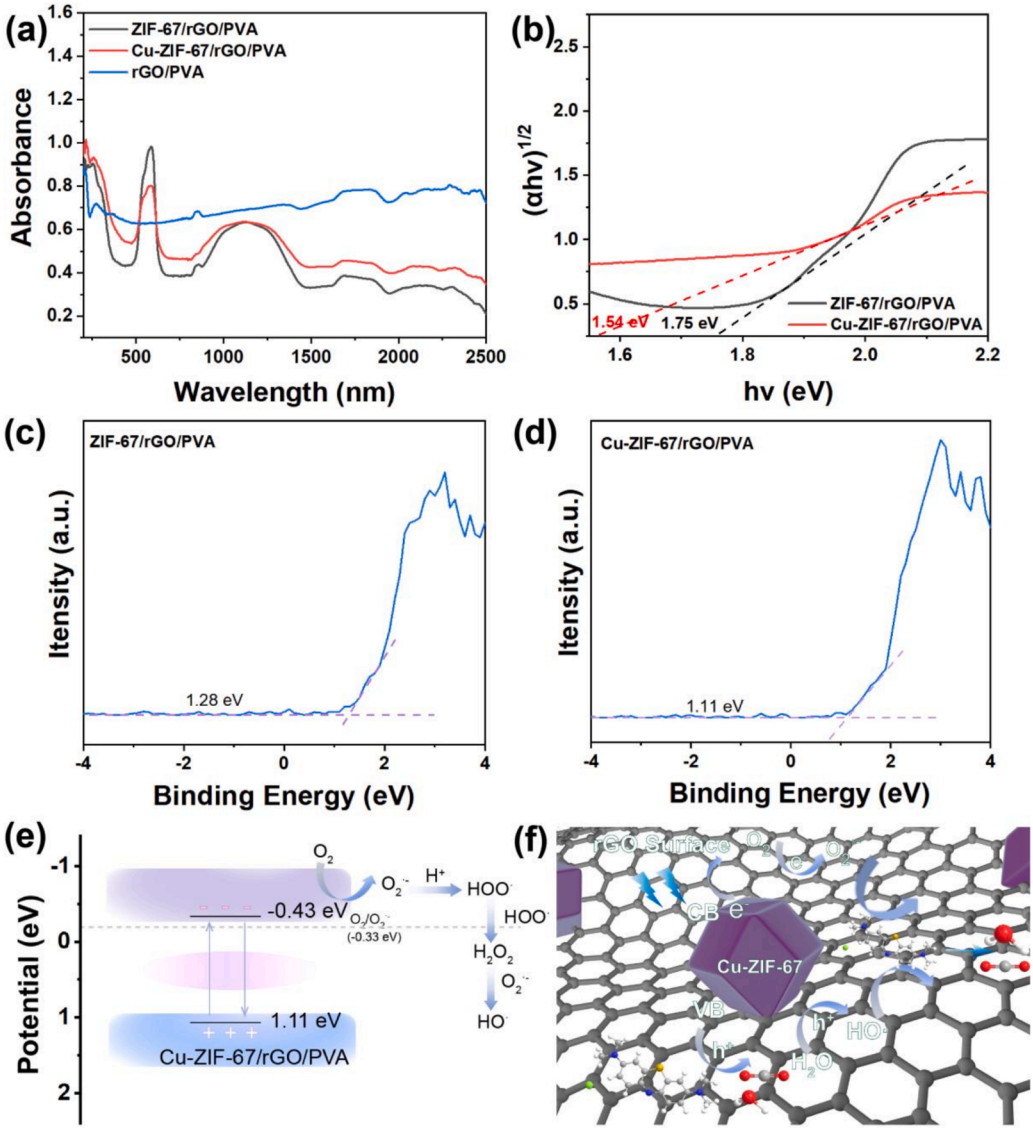

Fig. 8. a-b) UV-visible-infrared absorption spectra of rGO/PVA, ZIF-67/rGO/PVA and Cu-ZIF-67/rGO/PVA, and Tauc plots for rGO/PVA, ZIF-67/rGO/PVA, Cu-ZIF-67/rGO/PVA, XPS valence band spectroscopy of c) ZIF-67/rGO/PVA, d) Cu-ZIF-67/rGO/PVA, e) Schematic illustration of the electronic band structures of Cu-ZIF-67/rGO/PVA, f) Proposed mechanism for photocatalytic activity using Cu-ZIF-67/rGO/PVA.

potential of the Cu-ZIF-67/rGO/PVA for photocatalytic and electrocatalytic applications. According to the Kubelka-Munk formula, the $(ah\nu)^{1/2}$ vs. $h\nu$ correspondence curves of the direct bandgap are plotted and the straight-line portion is extrapolated along the $h\nu$ coordinates to obtain the forbidden bandwidths of 1.75 and 1.54 eV for ZIF-67/rGO/PVA and Cu-ZIF-67/rGO/PVA, respectively. The valance band maximum (VBM) values of ZIF-67/rGO/PVA and Cu-ZIF-67/rGO/PVA were 1.28 eV and 1.11 eV, respectively (Fig. 8c-d) [53]. According to these results, the energy band structures of Cu-ZIF-67/rGO/PVA are calculated and shown in Fig. 8e. Because of Cu doping, the band gap of Cu-ZIF-67/rGO/PVA is smaller than that of ZIF-67/rGO/PVA, which is easier to absorb solar excitation. CB potential of Cu-ZIF-67/rGO/PVA is lower than that of the $O_2/O_2^{\cdot-}$ formal potential (-0.33 V), suggesting that photo-excited electrons are effective in reducing O_2 to $O_2^{\cdot-}$, thus further degrading the pollutant. $O_2^{\cdot-}$ can also combine with H^+ to form hydrogen peroxide, which eventually breaks down to hydroxyl radicals ($HO^{\cdot}$) during reduction. The photocatalytic mechanism of Cu-ZIF-67/rGO/PVA composites is shown in Fig. 8f. In the Cu-ZIF-67/rGO/PVA composite, Cu-ZIF-67 functions as a generator of photogenerated electron-hole (e^- - h^+) pairs. At the same time, rGO serves as a carrier channel. Due to the heterogeneous structure in the Cu-ZIF-67/rGO composite, under visible light irradiation, e^- jumps from the valence band to the conduction band of Cu-ZIF-67 and rapidly transfers to the nearest surface of rGO, leaving more h^+ in the valence band of Cu-ZIF-67 and more e^- in the surface of rGO. e^- react with O_2 to generate superoxide radicals ($O_2^{\cdot-}$) [54,55]. Due to their potent oxidizing and reducing capabilities, $HO^{\cdot}$ and $O_2^{\cdot-}$ can degrade pollutants into smaller molecular weights and simpler intermediates, ultimately producing CO_2 and H_2O. In conclusion, Cu-ZIF-67/rGO/PVA demonstrated excellent photocatalytic activity and pollutant removal ability in photocatalytic degradation.

3.5. Solar-thermal and photocatalyst degradation mechanism

Fig. 9 illustrates the synergistic process of the Cu-ZIF-67/rGO/PVA, combining water evaporation and photocatalytic degradation. Cu-ZIF-67 loaded rGO/PVA aerogels (Cu-ZIF-67/rGO/PVA) were prepared by thermal reduction and surface growth. Cu-doped ZIF-67 has good light absorption properties. rGO can effectively absorb light energy and quickly convert it into heat, thus further improving the overall photothermal performance. The effective tuning of the energy band structure

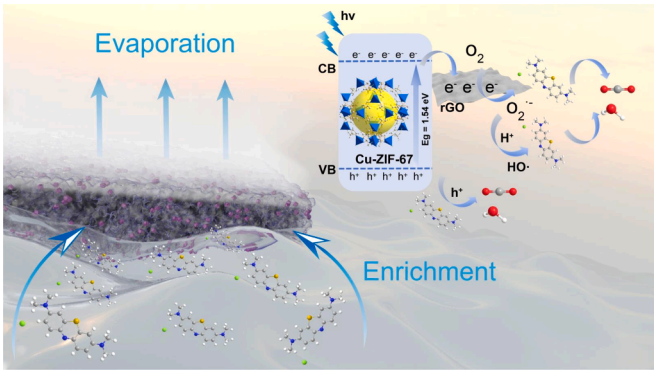

Fig. 9. Schematic illustrating the solar-thermal and photocatalytic mechanisms of the Cu-ZIF-67/rGO/PVA under solar light irradiation.

is crucial for the effective separation of photogenerated carriers, and a suitable energy band structure can significantly improve the catalytic activity of the photocatalyst. In the Cu-ZIF-67/rGO/PVA composites, Cu-ZIF-67 acts as a photogenerated electron-hole (e^- - h^+) pair generator, while rGO acts as a carrier channel. The heterostructure of Cu-ZIF-67 and rGO in the Cu-ZIF-67/PVA composites accelerated the electron separation and inhibited the compounding of photogenerated electrons and holes, significantly prolonging the initiation reaction lifetime. The adsorption of reactants on the surface of Cu-ZIF-67/rGO/PVA enhanced the photocatalytic activity. Cu-ZIF-67/rGO exhibits significant comprehensive performance advantages in solar-powered water purification by combining interfacial evaporation and photocatalytic degradation functions.

4. Conclusion

In this work, an aerogel evaporator was constructed by rGO and PVA, and Cu-ZIF-67 was evenly grown on its surface. Cu doping broadened the light absorption range of ZIF-67 and significantly improved the photocatalytic degradation efficiency. rGO not only performs well in the absorption of sunlight but also quickly transfers photogenerated electrons from Cu-ZIF-67 to the reaction interface, thereby effectively extending the lifetime of photogenerated electrons and holes and improving photocatalytic efficiency. Cu-ZIF-67/rGO/PVA has the advantages of broad light absorption, efficient photothermal conversion, and salt resistance. The evaporation rate under 1 sun can reach 1.95 kg m^{-2} h^{-1}, and it also has an excellent photocatalytic degradation effect on organic pollutants in water. This work lays the foundation for constructing an aerogel with synergistic photothermal evaporation and photocatalytic degradation properties to achieve sustainable remediation of water bodies.

CRediT authorship contribution statement

Fan Nie: Writing – original draft, Methodology, Investigation. **Jihai Cai:** Writing – review & editing, Data curation. **Lingxuan Ma:** Investigation. **Sheng Gong:** Formal analysis. **Shuangpeng Wang:** Writing – original draft, Conceptualization. **Wenqian Chen:** Validation, Methodology. **Shengliang Li:** Writing – review & editing, Conceptualization. **Jinchao Wei:** Writing – review & editing, Supervision, Funding acquisition, Conceptualization. **Peng Li:** Supervision, Project administration, Funding acquisition.

Declaration of competing interest

The authors declare that they have no known competing financial interests or personal relationships that could have appeared to influence the work reported in this paper.

Acknowledgment

We gratefully acknowledge the financial support from Macau Science and Technology Development Fund (0014/2022/ITP, 0031/2022/AGJ, 001/2023/ALC and 005/2023/SKL), Guangdong Basic and Applied Basic Research Foundation (2024A1515030214), and the Research Committee of the University of Macau (MYRG-CRG2022-00016-ICMS, SRG2022-00035-ICMS, and MYRG2023-00205-ICMS).

Appendix A. Supplementary data

Supplementary data to this article can be found online at https://doi.org/10.1016/j.cej.2024.159130.

Data availability

Data will be made available on request.

References

[1] J.Y. Lin, W.Y. Ye, M. Xie, D.H. Seo, J.Q. Luo, Y.H. Wan, B. van der Bruggen, Environmental impacts and remediation of dye-containing wastewater, Nat. Rev. Earth Environ. 4 (11) (2023) 785–803, https://doi.org/10.1038/s43017-023-00489-8.

[2] S. Parmar, S. Daki, S. Bhattacharya, A. Shrivastav, "Chapter 8 - Microorganism: an ecofriendly tool for waste management and environmental safety" in Development in Wastewater Treatment Research and Processes, M. P. Shah, S. Rodriguez-Couto, R. T. Kapoor, Eds. (Elsevier, 2022), pp. 175-193.

[3] R. Al-Tohamy, S.S. Ali, F. Li, K.M. Okasha, Y.A. Mahmoud, T. Elsamahy, H. Jiao, Y. Fu, J. Sun, A critical review on the treatment of dye-containing wastewater: Ecotoxicological and health concerns of textile dyes and possible remediation approaches for environmental safety, Ecotoxicol. Environ. Saf. 231 (2022) 113160, https://doi.org/10.1016/j.ecoenv.2021.113160.

[4] A. Sridhar, M. Ponnuchamy, A. Kapoor, S. Prabhakar, Valorization of food waste as adsorbents for toxic dye removal from contaminated waters: A review, J. Hazard. Mater. 424 (2022) 127432, https://doi.org/10.1016/j.jhazmat.2021.127432.

[5] S.Y. Ying, Z.Y. Liu, Y.R. Hu, R. Peng, X.S. Zhu, S.F. Dong, D. Yan, Y.X. Huang, Location-dependent occurrence and distribution of metal-based nanoparticles in bay environments, J. Hazard. Mater. 476 (2024) 134972, https://doi.org/10.1016/j.jhazmat.2024.134972.

[6] L. Lv, B. Yin, S. Zhang, W. Li, W. Gao, P. Wang, X. Liu, L. Sun, J. Liang, G. Zhang, Z. Ren, Review on intensified treatment of refractory wastewater in anaerobic digestion based on extracellular electron transfer: Mechanisms, strategies, and applications, Chem. Eng. J. 489 (2024) 151456, https://doi.org/10.1016/j.cej.2024.151456.

[7] M. Ahmadian, M. Jaymand, Interpenetrating polymer network hydrogels for removal of synthetic dyes: A comprehensive review, Coord. Chem. Rev. 486 (2023) 215152, https://doi.org/10.1016/j.ccr.2023.215152.

[8] S. Sarkar, N.T. Ponce, A. Banerjee, R. Bandopadhyay, S. Rajendran, E. Lichtfouse, Green polymeric nanomaterials for the photocatalytic degradation of dyes: a review, Environ. Chem. Lett. 18 (5) (2020) 1569–1580, https://doi.org/10.1007/s10311-020-01021-w.

[9] N. A. Nordin, M. A. Mohamed, M. N. I. Salehmin, S. F. Mohd Yusoff, Photocatalytic active metal–organic framework and its derivatives for solar-driven environmental remediation and renewable energy, Coord. Chem. Rev. 468 (2022) 214639, Doi: 10.1016/j.ccr.2022.214639.

[10] Z.Y. Zheng, S. Tian, Y.X. Feng, S. Zhao, X. Li, S.G. Wang, Z.L. He, Recent advances of photocatalytic coupling technologies for wastewater treatment, Chinese, J. Catal. 54 (2023) 88–136, https://doi.org/10.1016/S1872-2067(23)64536-X.

[11] E. Asayesh-Ardakani, M. Rahmani, A. Hosseinian, S.B. Ghaffari, M.H. Sarrafzadeh, Improvement strategies on application of covalent organic frameworks in adsorption, photocatalytic, and membrane processes for organic pollution removal from water, Coord. Chem. Rev. 518 (2024) 216087, https://doi.org/10.1016/j.ccr.2024.216087.

[12] R.R. Ikreedeegh, M.A. Hossen, A. Sherryna, M. Tahir, Recent advances on synthesis and photocatalytic applications of MOF-derived carbon materials: A review, Coord. Chem. Rev. 510 (2024) 215834, https://doi.org/10.1016/j.ccr.2024.215834.

[13] R. Gusain, K. Gupta, P. Joshi, O.P. Khatri, Adsorptive removal and photocatalytic degradation of organic pollutants using metal oxides and their composites: A comprehensive review, Adv. Colloid Interface Sci. 272 (2019) 102009, https://doi.org/10.1016/j.cis.2019.102009.

[14] Y.-H. Li, Z.-R. Tang, Y.-J. Xu, Multifunctional graphene-based composite photocatalysts oriented by multifaced roles of graphene in photocatalysis, Chinese J. Catal. 43 (3) (2022) 708–730, https://doi.org/10.1016/S1872-2067(21)63871-8.

[15] Z. Liu, D. Sun, C. Wang, B. You, B. Li, J. Han, S. Jiang, C. Zhang, S. He, Zeolitic imidazolate framework-67 and its derivatives for photocatalytic applications, Coord. Chem. Rev. 502 (2024) 215612, https://doi.org/10.1016/j.ccr.2023.215612.

[16] P. Mane, V. Burungale, H. Bae, C. Seong, J. Heo, S.-W. Ryu, S.-H. Kang, J.-S. Ha, Empowering metal oxide photoanodes via zeolitic imidazolate frameworks for efficient photoelectrochemical water splitting: Current advances and future perspectives, Renew. Sust. Energ. Rev. 202 (2024) 114671, https://doi.org/10.1016/j.rser.2024.114671.

[17] X. Wang, J. Hu, H. Guan, X. Dai, M. Wu, X. Wang, Wood-based catalytic filter decorated with ZIF-67 for highly efficient and continuous organic pollutant removal, Chem. Eng. J. 479 (2024) 147580, https://doi.org/10.1016/j.cej.2023.147580.

[18] L.F. Ning, X. Chen, Z.P. Wang, J. Xu, High-efficiency pollutant degradation, disinfection and H_2O_2 production activities of magnetically separable Co-imbedded N-doped carbonaceous framework/supramolecular perylene diimide photocatalyst, Appl. Catal. B 324 (2023) 122282, https://doi.org/10.1016/j.apcatb.2022.122282.

[19] R. Ren, G. Liu, J.Y. Kim, R.E.A. Ardhi, M.X. Tran, W. Yang, J.K. Lee, Photoactive g-C_3N_4/CuZIF-67 bifunctional electrocatalyst with staggered p-n heterojunction for rechargeable Zn-air batteries, Appl. Catal. B 306 (2022) 121096, https://doi.org/10.1016/j.apcatb.2022.121096.

[20] F. Dai, M. Zhang, Q. Chen, M. Mi, Z. Li, J. Han, J. Xing, S. Feng, L. Wang, Highly efficient CO_2 photoreduction by ultralow-Ru-Loading ZIF-67, Appl. Catal. B 336 (2023) 122934, https://doi.org/10.1016/j.apcatb.2023.122934.

[21] J. Zhang, H. Zeng, L. Bu, S. Zhou, Z. Shi, L. Deng, Cu_0 incorporated cobalt/nitrogen doped carbonaceous frameworks derived from ZIF-67 (Cu@Co-N-C) as PMS activator for efficient degradation of naproxen: Direct electron transfer and $^1O_2$ dominated nonradical mechanisms, Chem. Eng. J. 454 (2023) 139989, https://doi.org/10.1016/j.cej.2022.139989.

[22] S. Nazari, E. Asgari, A. Sheikhmohammadi, S.A. Mokhtari, H. Alamgholiloo, Visible-light-driven photocatalytic activity of WO3/ZIF-67 S-scheme heterojunction for upgrading degradation of oxytetracycline, J. Environ. Chem. Eng. 11 (5) (2023) 110393, https://doi.org/10.1016/j.jece.2023.110393.

[23] Y. He, G.T. Peng, Y. Jiang, M. Zhao, X.X. Wang, M.M. Chen, S.J. Lin, Environmental hazard potential of nano-photocatalysts determined by nano-bio interactions and exposure conditions, Small 16 (21) (2020) 1907690, https://doi.org/10.1002/smll.201907690.

[24] Y.L. Xu, X.F. Lu, G.J. Su, X. Chen, J. Meng, Q.Q. Li, C.X. Wang, B. Shi, Scientific and regulatory challenges of environmentally persistent free radicals: From formation theory to risk prevention strategies, J. Hazard. Mater. 456 (2023) 131674, https://doi.org/10.1016/j.jhazmat.2023.131674.

[25] Z.M. Liu, R.W. Liu, Y.B. Yi, W.J. Han, F.G. Kong, S.J. Wang, Photocatalytic degradation of dyes over a xylan/PVA/TiO_2 composite under visible light irradiation, Carbohyd. Polym. 223 (2019) 115081, https://doi.org/10.1016/j.carbpol.2019.115081.

[26] K. Jumnong, P. Kongseng, P. Maijan, S. Suwanboon, S. Chantarak, Double-function ZnO/starch biodegradable hydrogel composite for methylene blue adsorption and photocatalytic degradation, Int. J. Biol. Macromol. 253 (2023) 127533, https://doi.org/10.1016/j.ijbiomac.2023.127533.

[27] J. Wei, M. Yuan, S. Wang, X. Wang, N. An, G. Lv, L. Wu, Recent advances in metal organic frameworks for the catalytic degradation of organic pollutants, Collagen and Leather 5 (1) (2023) 33, https://doi.org/10.1186/s42825-023-00140-8.

[28] B. Xiang, J. Gong, Y. Sun, J. Li, Robust PVA/GO@MOF membrane with fast photothermal self-cleaning property for oily wastewater purification, J. Hazard. Mater. 462 (2024) 132803, https://doi.org/10.1016/j.jhazmat.2023.132803.

[29] Y. Nosaka, A.Y. Nosaka, Generation and detection of reactive oxygen species in photocatalysis, Chem. Rev. 117 (17) (2017) 11302–11336, https://doi.org/10.1021/acs.chemrev.7b00161.

[30] T. Xue, F. Yang, X. Zhao, F. He, Z. Wang, Q. Wali, W. Fan, T. Liu, Portable solar interfacial evaporator based on polyimide nanofiber aerogel for efficient desalination, Chem. Eng. J. 461 (2023) 141909, https://doi.org/10.1016/j.cej.2023.141909.

[31] D.Q. Fan, Y. Lu, H. Zhang, H.L. Xu, C.H. Lu, Y.C. Tang, X.F. Yang, Synergy of photocatalysis and photothermal effect in integrated 0D perovskite oxide/2D MXene heterostructures for simultaneous water purification and solar steam generation, Appl. Catal. B 295 (2021) 120285, https://doi.org/10.1016/j.apcatb.2021.120285.

[32] R. Meng, J. Lyu, Y. Lu, M. Salimi, B. Zhu, D.K. Macharia, L. Zhang, M. Amidpour, L. Zou, Z. Chen, Growth of phosphomolybdate-carbon hybrid nanorod array on carbon-fiber cloth with enhanced light-trapping and decreased water-evaporation enthalpy for constructing efficient salt-free hanging evaporator, Chem. Eng. J. 476 (2023) 146756, https://doi.org/10.1016/j.cej.2023.146756.

[33] R. Meng, J. Lyu, L. Zou, Q. Zhong, Z. Liu, B. Zhu, M. Chen, L. Zhang, Z. Chen, CNT-based gel-coated cotton fabrics for constructing symmetrical evaporator with up/down inversion property for efficient continuous solar desalination, Desalination 554 (2023) 116494, https://doi.org/10.1016/j.desal.2023.116494.

[34] W. Chong, R. Meng, Z. Liu, Q. Liu, J. Hu, B. Zhu, D.K. Macharia, Z. Chen, L. Zhang, Superhydrophilic polydopamine-modified carbon-fiber membrane with rapid seawater-transferring ability for constructing efficient hanging-model evaporator, Adv. Fiber Mater. 5 (3) (2023) 1063–1075, https://doi.org/10.1007/s42765-023-00276-6.

[35] C. Ge, D. Xu, H. Du, Z. Chen, J. Chen, Z. Shen, W. Xu, Q. Zhang, J. Fang, Recent advances in fibrous materials for interfacial solar steam generation, Adv. Fiber Mater. 5 (3) (2023) 791–818, https://doi.org/10.1007/s42765-022-00228-6.

[36] J. Zhao, Z. Liu, S.C. Low, Z. Xu, S.H. Tan, Electrospinning technique meets solar energy: electrospun nanofiber-based evaporation systems for solar steam generation, Adv. Fiber Mater. 5 (4) (2023) 1318–1348, https://doi.org/10.1007/s42765-023-00286-4.

[37] N. Li, S. Wu, H. Dai, Z. Cheng, W. Peng, B. Yan, G. Chen, S. Wang, X. Duan, Thermal activation of persulfates for organic wastewater purification: Heating modes, mechanism and influencing factors, Chem. Eng. J. 450 (2022) 137976, https://doi.org/10.1016/j.cej.2022.137976.

[38] Q. Hongxin, S. Xiaohao, W. Bozeng, S. Xinqian, H. Mingzhen, Y. Youming, Study on the influence of active oxygen on the natural oxidation of arsenopyrite under different temperature conditions, J. Hazard. Mater. 478 (2024) 135420, https://doi.org/10.1016/j.jhazmat.2024.135420.

[39] T.T. Zhang, J. Qu, J. Wu, F.Z. Jiao, C.J. Li, F.L. Gao, J. Liu, Z.Z. Yu, X.F. Li, All-in-one self-floating wood-based solar-thermal evaporators for simultaneous solar steam generation and catalytic degradation, Adv. Funct. Mater. 2403505 (2024), https://doi.org/10.1002/adfm.202403505.

[40] Q.H. Liao, P.P. Zhang, H.Z. Yao, H.H. Cheng, C. Li, L.T. Qu, Reduced graphene oxide-based spectrally selective absorber with an extremely low thermal emittance and high solar absorptance, Adv. Sci. 7 (8) (2020) 1903125, https://doi.org/10.1002/advs.201903125.

[41] B.P. Zhang, P.W. Wong, A.K. An, Photothermally enabled MXene hydrogel membrane with integrated solar-driven evaporation and photodegradation for efficient water purification, Chem. Eng. J. 430 (2022) 133054, https://doi.org/10.1016/j.cej.2021.133054.

[42] T.N. Ghosh, A.K. Bhunia, S.S. Pradhan, S.K. Sarkar, Electric modulus approach to the analysis of electric relaxation and magnetodielectric effect in reduced graphene oxide-poly(vinyl alcohol) nanocomposite, J. Mater. Sci. Mater. Electron. 31 (18) (2020) 15919–15930, https://doi.org/10.1007/s10854-020-04153-5.

[43] R.D. Shannon, Revised effective ionic radii and systematic studies of interatomic distances in halides and chalcogenides, Acta Crystallogr. A 32 (5) (1976) 751–767, https://doi.org/10.1107/S0567739476001551.

[44] J. A. MartÍnez-DÍez, M. A. RodrÍguez-PÉRez, J. A. De Saja, L. O. Arcos Y RÁbago, O. A. Almanza, The thermal conductivity of a polyethylene foam block produced by a compression molding process, Journal of Cellular Plastics 37(1) (2001) 21-42, Doi: 10.1106/D0MJ-HJH8-5YDQ-H5VB.

[45] W. Li, X. Li, W.-J. Chang, J. Wu, P. Liu, J. Wang, X. Yao, Z. Yu, Vertically aligned reduced graphene oxide/Ti_3C_2Tx MXene hybrid hydrogel for highly efficient solar steam generation, Nano Research 13 (2020) 3048–3056, https://doi.org/10.1007/s12274-020-2970-y.

[46] Z.T. Li, J. Zhang, S.H. Zang, C. Yang, Y. Liu, F. Jing, H. Jing, J.K. Hu, C.B. Wang, Y. T. Zhou, Engineering controllable water transport of biosafety cuttlefish juice solar absorber toward remarkably enhanced solar-driven gas-liquid interfacial evaporation, Nano Energy 73 (2020) 104834, https://doi.org/10.1016/j.nanoen.2020.104834.

[47] M.R. Wu, Y. Wei, Y.Q. Zhu, Y.F. Bai, Y.T. Wang, X.M. Wang, S.H. Ho, W. Wang, R. X. Li, Hydrophilic polymer foam as a monolithic interfacial solar evaporator with rapid self-cleaning, high evaporation efficiency, and salt resistance, Adv. Funct. Mater. 2410729 (2024), https://doi.org/10.1002/adfm.202410729.

[48] J. Zhao, K. Yu, Y. Hu, S. Li, X. Tan, F. Chen, Z. Yu, Discharge behavior of Mg–4wt% Ga–2wt%Hg alloy as anode for seawater activated battery, Electrochimica Acta 56 (24) (2011) 8224–8231, https://doi.org/10.1016/j.electacta.2011.06.065.

[49] J. Zhang, W. Hu, S. Cao, L. Piao, Recent progress for hydrogen production by photocatalytic natural or simulated seawater splitting, Nano Research 13 (9) (2020) 2313–2322, https://doi.org/10.1007/s12274-020-2880-z.

[50] H. Luo, J. Wang, J. Chen, X. Li, Ag QDs modified BiOCl/UiO-66-NH_2 Z-scheme heterojunction for accelerated visible light-driven photocatalytic degradation of ciprofloxacin, J. Environ. Chem. Eng. 12 (6) (2024) 114299, https://doi.org/10.1016/j.jece.2024.114299.

[51] J. Wang, S. Wang, Effect of inorganic anions on the performance of advanced oxidation processes for degradation of organic contaminants, Chem. Eng. J. 411 (2021) 128392, https://doi.org/10.1016/j.cej.2020.128392.

[52] Z.T. Zhou, K.X. Li, W.Y. Deng, J. Li, Y.H. Yan, Y.W. Li, X.K. Quan, T. Wang, Nitrogen vacancy mediated exciton dissociation in carbon nitride nanosheets: Enhanced hydroxyl radicals generation for efficient photocatalytic degradation of organic pollutants, J. Hazard. Mater. 387 (2020) 122023, https://doi.org/10.1016/j.jhazmat.2020.122023.

[53] H.Y. Xie, K. Wang, D.Z. Xiang, S.L. Li, Z.L. Jin, Enwrapping graphdiyne (g-C_nH_{2n-2}) on hollow $NiCo_2O_4$ nanocages derived from a Prussian blue analogue as a p–n heterojunction for highly efficient photocatalytic hydrogen evolution, J. Mater. Chem. A 11 (27) (2023) 14971–14989, https://doi.org/10.1039/D3TA02598E.

[54] J.Q. Pan, Z.J. Dong, B.B. Wang, Z.Y. Jiang, C. Zhao, J.J. Wang, C.S. Song, Y. Y. Zheng, C.R. Li, The enhancement of photocatalytic hydrogen production via Ti^{3+} self-doping black TiO_2/g-C_3N_4 hollow core-shell nano-heterojunction, Appl. Catal. B 242 (2019) 92–99, https://doi.org/10.1016/j.apcatb.2018.09.079.

[55] L.Z. Chen, X.T. Xie, X.L. Song, S.C. Luo, S.Y. Ye, W.B. Situ, Photocatalytic degradation of ethylene in cold storage using the nanocomposite photocatalyst MIL101(Fe)-TiO_2-rGO, Chem. Eng. J. 424 (2021) 130407, https://doi.org/10.1016/j.cej.2021.130407.